J|A|C|S COMMUNICATIONS

Published on Web 12/01/2010

Core−Shell-Structured Magnetic Ternary Nanocubes

Lingyan Wang,[†] Xin Wang,[†] Jin Luo,[†] Bridgid N. Wanjala,[†] Chongmin Wang,[‡] Natasha A. Chernova,[†] Mark H. Engelhard,[‡] Yao Liu,[†] In-Tae Bae,[†] and Chuan-Jian Zhong*,[†]

Department of Chemistry, State University of New York at Binghamton, Binghamton, New York 13902, United States, and EMSL, Pacific Northwest National Laboratory, Richland, Washington 99352, United States

Received October 10, 2010; E-mail: cjzhong@binghamton.edu

Abstract: We report a novel core−shell-structured ternary nanocube of MnZn ferrite synthesized by controlling the reaction temperature and composition in the absence of conventionally used reducing agents. The highly monodispersed core−shell structure consists of an Fe_3O_4 core and an MnZn Ferrite shell. The observation of a Moiré pattern indicates that the core and the shell are two highly crystalline materials with slightly different lattice constants that are rotated relative to each other by a small angle. The ternary core−shell nanocubes display magnetic properties regulated by a combination of the core−shell composition and exhibit an increased coercivity and field-cooled/zero-field-cooled characteristics drastically different from those of regular MnZn ferrite nanoparticles. The ability to engineer the spatial nanostructures of ternary magnetic nanoparticles in terms of shape and composition offers atomic-level versatility in fine-tuning the nanoscale magnetic properties.

The metal dopant substitution of metal ferrite nanoparticles constitutes an important strategy for achieving high and tunable nanomagnetism. MnZn ferrite nanomaterials with a spinel structure represent an important class of such tunable magnetic materials that has attracted increasing interest.[1−3] The syntheses of MnZn ferrites[4−7] have largely been based on methods developed for fabricating bulk magnetic materials for solid-state applications, which are inadequate for applications involving biomolecular separation, specific targeting, or catalytic reactions in fuel cells and batteries. A key to the exploitation of MnZn ferrite nanoparticles in these applications is the ability to control the size, composition, and shape for tuning of the electronic, optical, and magnetic properties. In comparison with the synthesis of MnZn ferrite nanoparticles (20−40 nm) in aqueous solution,[8] the synthesis of metal or metal oxide nanoparticles in nonaqueous solutions has attracted a wide range of interest because it affords improved control over size and shape.[9−12] One of the documented strategies involves the use of oleic acid and/or oleylamine as a capping agent, metal acetylacetonates as metal precursors, and 1,2-hexadecanediol as a reducing agent.[9] This strategy was demonstrated for the synthesis of binary MFe_2O_4 (M = Fe, Co, Mn, Zn, etc.) nanoparticles with controllable sizes and shapes.[12,13] The synthesis of 8−12 nm cubelike and polyhedron-shaped binary $MnFe_2O_4$ nanoparticles from $Fe(acac)_3$ and $Mn(acac)_2$ in the presence of 1,2-hexadecanediol, oleic acid, and oleylamine represents an example where the shape control was achieved by the amount of stabilizers.[13] However, shape and composition control has rarely been demonstrated for ternary MnZn ferrite nanoparticles.[14,15] None of the prior studies have demonstrated control of the shape and spatial arrangement of the composition in the nanostructures.

Here we report a novel core−shell-structured nanocube of MnZn ferrite that was synthesized by controlling the reaction temperature and composition in the absence of conventional reducing agents in a one-pot synthesis. The highly monodispersed and cube-shaped core−shell structure consists of an Fe_3O_4 core and a $(Mn_{0.5}Zn_{0.5})(Fe_{0.9}Mn_{1.1})O_4$ shell. We show comparisons of MnZn ferrite core−shell nanocubes [e.g., $(Mn_{0.25}Zn_{0.25}Fe_{0.5})Fe_2O_4$ and (Fe_3O_4 core)−($Mn_{0.5}Zn_{0.5}$ shell) $(Fe_{0.9}Mn_{1.1})O_4$] with similar spinel structures of single and binary systems (e.g., $MnFe_2O_4$, $ZnFe_2O_4$, and Fe_3O_4/Fe_2O_3), focusing on understanding the morphologies, structures, and magnetic properties. Our discovery of this novel core−shell nanocube is interesting for two significant reasons. First, the synthesis of the shape-controlled core−shell magnetic nanoparticles was different from those reported previously[12,13] because of the elimination of reducing agents. Second, the core and shell were kept in the same cubic shape, even though their compositions were different. While an epitaxial relationship between the core and shell is favorable, the growth is determined by the crystal structures.[16,17] Despite the demonstration of other core−shell nanoparticles,[16−22] there have been no prior examples of cube-shaped core−shell MnZn ferrite nanoparticles.

For our cube-shaped core−shell MnZn ferrite nanoparticles, there are two major morphological features: the cubic shape with high monodispersity (Figure 1a) and the core−shell structure in the nanocube (Figure 1b,c). The synthesis involved a 0.7:0.3:2.0 Mn/Zn/:Fe feeding ratio and direct heating of the reaction solution at 270 °C followed by reflux for 1.5 h. Compositional analysis of the as-synthesized nanoparticles using direct-current plasma atomic emission spectrometry (DCP-AES) and X-ray photoelectron spectroscopy (XPS) yielded an Mn/Zn/Fe composition ratio of 4.9:1.3:7.0. Both the inner core and outer shell display ordered structures, with a relative core-to-shell volume ratio of ∼1:2. The core−shell structure is vividly revealed by the Moiré pattern of the core region of the particle (Figure 1b), which is formed by overlap of the core and the shell. In general, Moiré patterns originate from translational or rotational interference. The former arises when two crystals have parallel reflecting planes with a small difference in lattice parameters, and the latter occurs when two identical crystal spacings have a slight angular rotation.[16,21−25] In our case, the formation of the Moiré pattern also indicates that the core and the shell are both crystalline but have slightly different lattice constants or a certain degree of rotation of the core crystal relative to the shell. Various Moiré patterns have previously been reported for Pt−Pd core−shell nanocubics, MnO−Mn_3O_4 core−shell nanocrystals, and other nanostructures.[16,21,22] The measured lattice fringes for the outer shell are 0.217 and 0.300 nm, corresponding to the (400) and (220) planes of the spinel structure, respectively. These values are similar

[†] State University of New York at Binghamton.
[‡] Pacific Northwest National Laboratory.

10.1021/ja1091084

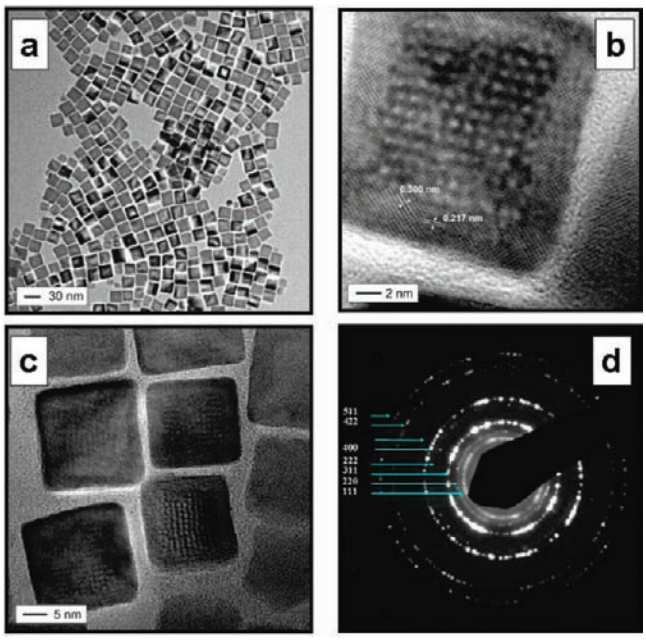

Figure 1. Morphologies of the MnZn ferrite core−shell nanocubes: (a) TEM image, (b, c) HRTEM images, and (d) electron diffraction pattern for a sample of as-synthesized MnZn ferrite nanoparticles [size = 20.6 ± 1.8 nm; Fe_3O_4 core; $(Mn_{0.5}Zn_{0.5})(Fe_{0.9}Mn_{1.1})O_4$ shell].

to the lattice fringes reported recently for 15 nm sized spherical $(Zn_{0.4}Fe_{0.6})Fe_2O_4$ nanoparticles synthesized by other methods.[26]

For the core, it is not straightforward to measure the lattice spacing from the HRTEM image because of the Moiré pattern. However, on the basis of an analysis of the electron diffraction pattern of a single particle, the core and the shell were found to be rotated by ~3° relative to each other. This accounts for the measured Moiré spacing of 1.17 nm, which is approximately perpendicular to the (220) lattice fringe. It is rather intriguing to observe the relative rotation of the shell with respect to the core, which is related to the relaxation of the lattice mismatch between the core and the shell. Similar rotation features have been reported for $MgO-YBa_2Cu_3O_{6.66}$ core−shell nanowires and $MnO-Mn_3O_4$ core−shell nanoparticles.[21,22] On the basis of the electron diffraction pattern (Figure 1d), the diffraction rings can be indexed in terms of the MnZn ferrite spinel phase, which will be shown later to agree well with the X-ray diffraction (XRD) results. As will be further discussed later, this core−shell-structured nanocube consists of an Fe_3O_4 core and a $(Mn_{0.5}Zn_{0.5})(Fe_{0.9}Mn_{1.1})O_4$ shell.

For MnZn ferrite nanoparticles synthesized similarly but using a different Mn/Zn/Fe feed ratio of 0.5:0.5:2.0, the compositional analysis of the as-synthesized nanoparticles yielded an Mn/Zn/Fe composition of 8.0:9.0:83.0. In this case, the cube-shaped particles have a size similar to the previous case but exhibit slightly distorted or irregular corners (Figure 2a).

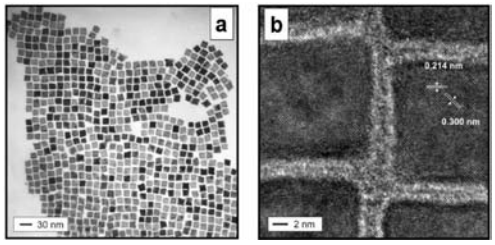

Figure 2. Morphologies of the MnZn ferrite core−shell nanocubes obtained under different synthesis conditions: (a) TEM and (b) HRTEM images.

There is no apparent core−shell structure, but a thin layer of shell structure seems to be identifiable along the edges of the nanocube. The measured lattice fringes of the nanocubes are 0.214 and 0.300 nm (Figure 2b), corresponding to the (400) and (220) planes of the spinel structure, which are practically identical to those observed for shell structure in Figure 1. We determined the composition as $(Mn_{0.25}Zn_{0.25}Fe_{0.5})Fe_2O_4$, as will be shown by the results from the structural and compositional analyses. We also note that our additional experimental results indicated that both the reaction time and temperature had effects on the size, shape, and structure of the as-synthesized nanoparticles, and there appeared to be an optimal temperature for the formation of the core−shell nanocubes. Further in-depth work is needed to establish their correlation with the reaction time and temperature.

To understand the above morphological and structural characteristics, we also examined other single- or two-component ferrite nanoparticles (e.g., $MnFe_2O_4$, $ZnFe_2O_4$, and Fe_3O_4 or Fe_2O_3) synthesized under the same conditions. Figure 3a shows an example of $MnFe_2O_4$ nanoparticles that were synthesized under identical conditions with a Mn/Fe feed ratio of 1.0:2.0. The as-synthesized nanoparticles showed an average size of 16 nm with a Mn/Fe ratio of 57.0:43.0, corresponding to $Mn(Fe_{1.25}Mn_{0.75})O_4$. Different shapes were observed, including spheres, cubes, hexagons, etc., though shapes characteristic of octahedrons and cubes seemed to be predominant. The measured lattice fringes are 0.302 and 0.480 nm, corresponding to the (220) and (111) planes, respectively.

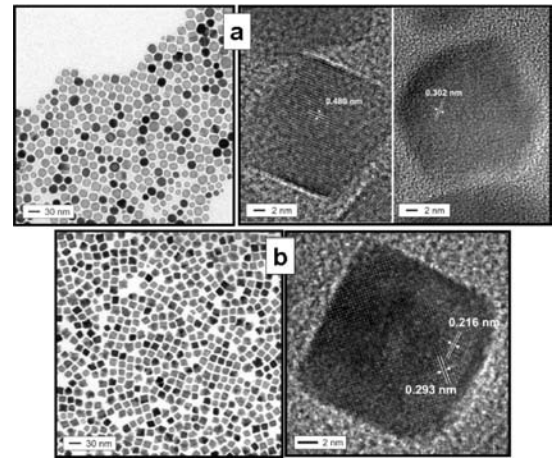

Figure 3. Morphologies of binary Mn or Zn ferrite nanoparticles: (left) TEM and (right) HRTEM images for (a) $Mn(Fe_{1.25}Mn_{0.75})O_4$ and (b) $(Zn_{0.24}Fe_{0.76})Fe_2O_4$ nanoparticles.

Figure 3b shows an example of $ZnFe_2O_4$ nanoparticles synthesized with a Zn/Fe feed ratio of 1.0:2.0. The as-synthesized nanoparticles (average size ~16 nm) was determined to have an Zn:Fe ratio of 8.0:92.0, corresponding to $(Zn_{0.24}Fe_{0.76})Fe_2O_4$. The morphology is largely characteristic of cubes with distorted features or small-sized particles at the corners of the cubes. The measured lattice fringes of 0.216 and 0.293 nm correspond to the (400) and (220) planes of the spinel structure, respectively. Fe_3O_4 nanoparticles were also synthesized and showed morphologies and structures consistent with those reported earlier.[18,27] For example, the determined lattice fringe (0.480 nm) corresponds to the (111) plane of the spinel structure.[27]

In Figure 4, we show a representative set of XRD patterns for as-synthesized nanoparticles, including (a) $(Mn_{0.25}Zn_{0.25}Fe_{0.5})Fe_2O_4$, (b) $Mn(Fe_{1.25}Mn_{0.75})O_4$, (c) ($Fe_3O_4$ core)−[$(Mn_{0.5}Zn_{0.5})(Fe_{0.9}Mn_{1.1})O_4$ shell], and (d) Fe_3O_4. As indexed in the XRD patterns, the nanoparticles display the spinel structure,[6] which is consistent with

those reported in the literature for this class of materials.[12,13,27−29] Remarkably, the relative intensity ratios of the (400) and (440) peaks versus the (311) peak were found to be much higher for the (Fe_3O_4 core)−[($Mn_{0.5}Zn_{0.5}$)($Fe_{0.9}Mn_{1.1}$)O_4 shell] nanoparticles than those for the ($Mn_{0.25}Zn_{0.25}Fe_{0.5}$)$Fe_2O_4$, $Mn(Fe_{1.25}Mn_{0.75})O_4$, and Fe_3O_4 nanoparticles. This finding is consistent with the predominant cubic shape for the core−shell nanocubes.[13] It may also in part reflect the difference in electronic density on tetrahedral and octahedral sites. The extracted average lattice constants were found to be 0.839 nm for Fe_3O_4 nanoparticles,[18,27] 0.855 nm for $Mn(Fe_{1.25}Mn_{0.75})O_4$ nanoparticles, and 0.857 nm for ($Mn_{0.25}Zn_{0.25}Fe_{0.5}$)$Fe_2O_4$ nanoparticles. A separate measurement yielded a value of 0.841 nm for ($Zn_{0.24}Fe_{0.76}$)Fe_2O_4 nanoparticles.

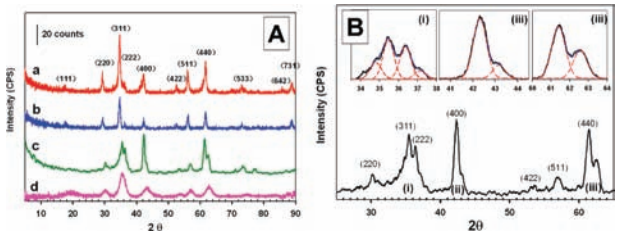

Figure 4. Structural analysis of the different ferrite nanoparticles. (A) XRD patterns for four different samples: (a) ($Mn_{0.25}Zn_{0.25}Fe_{0.5}$)$Fe_2O_4$; (b) $Mn(Fe_{1.25}Mn_{0.75})O_4$; (c), ($Fe_3O_4$ core)−[($Mn_{0.5}Zn_{0.5}$)($Fe_{0.9}Mn_{1.1}$)O_4 shell]; (d) Fe_3O_4. (B) Deconvolution results for pattern (c) in three peak regions.

Upon close examination of the XRD pattern for the core−shell nanocubes (c), we found subtle differences from the other patterns in terms of peak shoulder or double peak characteristics. The subtle differences are believed to reflect the presence of different phases in this nanostructure. While it is possible that the XRD pattern could be due to a simple mixing of Fe_3O_4 and MnZn ferrite, the high monodispersity of the nanocubes observed in the TEM images (Figure 1a) suggests that having such a simple mixture in the sample is unlikely. By deconvolution of the XRD pattern, double peaks are clearly revealed for the (311), (222), (400), and (440) peaks, yielding two sets of peak patterns [see the Figure 4B inset and Table S1 in the Supporting Information (SI)]. The lattice constant for the deconvoluted peak at the higher diffraction angle is 0.838 nm, in close agreement with that for Fe_3O_4,[18,27] whereas the lattice constant for the deconvoluted peak at the lower diffraction angle is 0.854 nm, which is close to that for the MnZn ferrite.[29] Moreover, the results also reveal the difference in the relative intensity (I) ratios for the major peaks of (400) and (440) versus (311). The relative peak intensity ratios [I(400)/I(440)/I(311)] were found to be about 4:3:1 and 1:2:4, respectively.

The above results are indicative of the presence of two different phases in the core−shell nanocube, which is believed to consist of an Fe_3O_4 core and a MnZn ferrite ($Mn_{0.5}Zn_{0.5}$)($Fe_{0.9}Mn_{1.1}$)O_4 shell. The substitution of Mn and Zn in the spinel cell should increase the lattice constant, as expected on the basis of earlier studies of similar spinel structures.[29] For the mixed oxide spinels, it is often problematic to determine the valences and distributions of the cations among the tetrahedral (tet) and octahedral (oct) sites of the spinel structure. This can also be particularly problematic if the different cations can adopt more than one valence state. We used XPS to probe the oxidation states of the ions. From the XPS analysis (see the SI) and the Mn/Zn/Fe composition, the nanocubes were determined to be rich in Mn. The Mn $2p_{3/2}$ and $2p_{1/2}$ bands were detected at 641.4 and 653.1 eV, indicating that Mn may be present mostly as Mn^{3+},[30] in addition to a satellite peak associated with Mn^{2+}. The Zn $2p_{3/2}$ band was detected at 1021.6 eV, agreeing with the reported value for Zn^{2+}.[30] The Fe $2p_{3/2}$ and $2p_{1/2}$ bands were detected at 711.1 and 724.9 eV, which are slightly higher (by 0.1 eV) than those reported previously for Fe_3O_4 (711.0 and 724.8 eV[18,27]). The observed satellite peak between the two peaks is also indicative of the presence of Fe^{3+}. These results suggest the presence of both Mn^{3+} and Fe^{3+} in the nanoparticles. The possibility of oxidation of Mn^{2+} to Mn^{3+} is supported by the XPS data (see the SI). Such a partial oxidation could lead to diffusion of part of the metal ions out to the shell structure. The observation of similar structural features was reported previously for Fe/Fe_2O_3 nanoparticles.[31−33] A core composition of Fe_3O_4 and a shell composition of ($Mn_{0.5}Zn_{0.5}$)($Fe_{0.9}Mn_{1.1}$)O_4 were thus derived from the high-resolution transmission electron microscopy (HRTEM), XRD, and XPS data, which are qualitatively consistent with the fact that the three elements Fe, Mn, and Zn have similar atomic weights and the core and the shell have close lattice constants and similar densities. In view of the penetration depth of XPS (∼5 nm), it is possible that not all of the Fe species inside the core of the 20 nm particle were detected. Furthermore, the particle sizes of 20−24 nm calculated from the deconvoluted XRD peak widths using the Scherrer equation (see the SI) are comparable with the core and shell sizes determined from the TEM data (∼20 nm).

Scheme 1. Structural Model for the MnZn Ferrite Nanocubes[a]

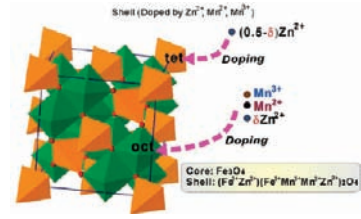

[a] The structure consists of an Fe_3O_4 core (inverse-spinel) and MnZn ferrite shell. The tetrahedral sites are doped with (0.5 − δ) Zn^{2+}, whereas the octahedral sites are doped with Mn^{3+}, Mn^{2+}, and the remaining Zn^{2+}.

Scheme 1 illustrates the structure for the core−shell nanocube consisting of an Fe_3O_4 core and a MnZn ferrite shell. Such ferrites can be either antiferromagnetic or ferrimagnetic because the magnetic spins of ions on the tetrahedral sites are antiparallel to those on the octahedral sites.[34] Since Fe_3O_4 is inverse-spinel, the tetrahedral sites are occupied by Fe^{3+} whereas the octahedral sites are occupied by Fe^{2+} and Fe^{3+}, resulting in a saturation magnetization of 4 μ_B/formula unit or ∼96.5 emu/g. In the MnZn ferrite shell, the structure could have the tetrahedral and octahedral sites occupied by different levels of Fe^{3+} and Zn^{2+}, with larger-sized Fe^{2+} and Mn^{2+} as well as Jahn−Teller-active Mn^{3+} usually preferring octahedral sites.[35,36] The bulk zinc ferrite synthesized at high temperature is a normal spinel with Zn^{2+} at the tetrahedral sites, but low-temperature synthesis routes leading to zinc ferrite nanoparticles reportedly result in partially inverse $[Zn_{1-\delta}Fe_\delta]^{tet}[Zn_\delta Fe_{2-\delta}]^{oct}O_4$ spinel, with the inversion parameter δ dependent upon the synthesis conditions.[37]

The magnetic properties of the core−shell nanocubes were examined in terms of saturation magnetization, coercivity, susceptibility, and blocking temperature by means of superconducting quantum interference device (SQUID) measurements. The saturation magnetization values were measured at 100 K with an applied field of −50 to 50 kOe. Figure 5a shows the magnetization hysteresis for the (Fe_3O_4 core)−[($Mn_{0.5}Zn_{0.5}$)($Fe_{0.9}Mn_{1.1}$)O_4 shell] nanocubes. The highest magnetization value was found to be 45.6 emu/g, corresponding to ∼1.9 μ_B/formula unit. Notably, the maximum magnetization value for 5.2 nm Fe_3O_4 was previously reported to be 66 emu/g.[18] Intuitively, the saturation magnetization in Fe_3O_4 increases with Zn substitution at the tetrahedral sites and decreases

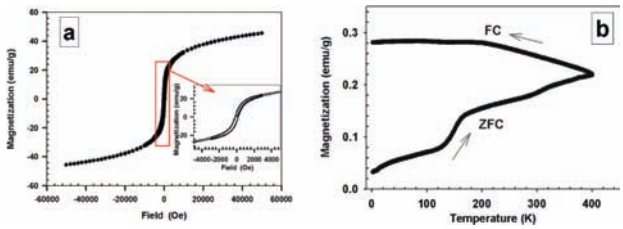

Figure 5. Magnetization curves for (Fe_3O_4 core)−[($Mn_{0.5}Zn_{0.5}$)-($Fe_{0.9}Mn_{1.1}$)O_4 shell] nanocubes: SQUID measurements of (a) magnetization hysteresis curves and (b) field-cooled (FC) and zero-field-cooled (ZFC) curves.

when Zn goes to the octahedral sites. However, only a crystallographically infeasible structure with nearly all of the Zn^{2+} at octahedral sites would produce such a low saturation magnetization. Thus, the site distribution of ions in the shell can be expressed as $(Zn^{2+}{}_{0.5-\delta}Fe^{3+}{}_{0.5+\delta})^{tet}(Mn^{2+}{}_{0.5}Mn^{3+}{}_{1.1}Fe^{3+}{}_{0.4-\delta}Zn_{\delta})^{oct}O_4$ on the basis of our structural and magnetic analysis, with the inversion δ being significant. The precise value of δ has not yet been determined.

The saturation magnetization can also be lowered by a demagnetizing interaction between the Fe_3O_4 core and the MnZn ferrite shell. Interestingly, we found that the coercivity value was ∼350 Oe for the core−shell nanocubes at 100 K, which was much higher than that for Fe_3O_4 nanoparticles at 5 K (40 Oe).[18] This is consistent with the earlier assumption of a magnetic interaction between the core and the shell. In the ZFC curve (Figure 5b), the magnetization initially shows a slow increase with temperature, followed by a rapid increase from ∼120 to 170 K. After this, the magnetization increase slowed, and there was no indication that a maximum had been reached by 400 K. This type of FC/ZFC trend may be indicative of the presence of two magnetic phases in the sample. It is interesting to note that Fe_3O_4 nanoparicles of similar size to our Fe_3O_4 core show a blocking temperature of ∼100 K,[38] i.e., over similar temperature interval where the most rapid ZFC magnetization growth was observed. This suggests that the core becomes superparamagnetic above 120−170 K, while the larger shell stays blocked up to at least 400 K.[38,39] Blocking temperatures over 350 K were previously reported for $Mn_{1-x}Zn_xFe_2O_4$ nanoparticles with high manganese content.[29] In the FC curve (Figure 5b), the magnetization initially showed a slow increase with decreasing temperature until it became stable in the 200−2 K range, suggesting an overall ferrimagnet-like behavior.[39]

In summary, we have synthesized highly monodispersed core−shell nanocubes consisting of an Fe_3O_4 core and an ($Mn_{0.5}Zn_{0.5}$)-($Fe_{0.9}Mn_{1.1}$)O_4 shell. The core and the shell are highly crystalline nanostructures with slightly different lattice constants. The core−shell-structured nanocubes display unique magnetic properties regulated by a combination of the core−shell composition, leading to a higher coercivity (∼350 Oe) and FC/ZFC characteristics drastically different from those of many regular MnZn ferrite nanoparticles. We expect that a detailed delineation of size, composition, and shape for this class of core−shell nanocubes could lead to the design of advanced nanostructures useful for magnetic and catalytic applications.

Acknowledgment. This work was supported by NSF (CHE 0848701, CBET 0709113). The XPS and some HRTEM were performed using the EMSL User Facility of the DOE at PNNL.

Supporting Information Available: Additional details for the synthesis, measurement, and data. This material is available free of charge via the Internet at http://pubs.acs.org.

References

(1) Zaspalis, V.; Tsakaloudi, V.; Papazoglou, E.; Kolenbrander, M.; Guenther, R.; Van Der Valk, P. *J. Electroceram.* **2004**, *13*, 585–591.
(2) Shokrollahi, H.; Janghorban, K. *J. Mater. Process. Technol.* **2007**, *189*, 1–12.
(3) Goldman, A. *Modern Ferrite Technology*; Van Nostrand-Reinhold: New York, 1990.
(4) Kosak, A.; Drofenik, M.; Znidarsic, A. *J. Magn. Magn. Mater.* **2004**, *272*, 1542–1544.
(5) Makovec, D.; Kosak, A.; Drofenik, M. *Nanotechnology* **2004**, *15*, 160–166.
(6) Kosak, A.; Makovec, D.; Znidarsic, A.; Drofenik, M. *J. Eur. Ceram. Soc.* **2004**, *24*, 959–962.
(7) Verma, S.; Joy, P. A.; Khollam, Y. B.; Potdar, H. S.; Deshpande, S. B. *Mater. Lett.* **2004**, *58*, 1092–1095.
(8) Wang, X.; Wang, L.; Lim, S. I.-I.; Bao, K.; Mott, D.; Park, H.-Y.; Luo, J.; Hao, S.; Zhong, C. J. *J. Nanosci. Nanotechnol.* **2009**, *9*, 3005–3012.
(9) Sun, S.; Murray, C.; Weller, D.; Folks, L.; Moser, A. *Science* **2000**, *287*, 1989–1992.
(10) Jana, N. R.; Chen, Y. F.; Peng, X. G. *Chem. Mater.* **2004**, *16*, 3931–3935.
(11) Park, J.; An, K. J.; Hwang, Y. S.; Park, J. G.; Noh, H. J.; Kim, J. Y.; Park, J. H.; Hwang, N. M.; Hyeon, T. *Nat. Mater.* **2004**, *3*, 891–895.
(12) Sun, S.; Zeng, H.; Robinson, D. B.; Raoux, S.; Rice, P. M.; Wang, S. X.; Li, G. *J. Am. Chem. Soc.* **2004**, *126*, 273–279.
(13) Zeng, H.; Rice, P. M.; Wang, S. X.; Sun, S. *J. Am. Chem. Soc.* **2004**, *126*, 11458–11459.
(14) Parekh, K.; Upadhyay, R.; Belova, L.; Rao, K. *Nanotechnology* **2006**, *17*, 5970–5975.
(15) Jang, J.; Nah, H.; Lee, J.; Moon, S.; Kim, M.; Cheon, J. *Angew. Chem., Int. Ed.* **2009**, *48*, 1234–1238.
(16) Habas, S.; Lee, H.; Radmilovic, V.; Somorjai, G.; Yang, P. *Nat. Mater.* **2007**, *6*, 692–697.
(17) Li, J.; Zeng, H.; Sun, S.; Liu, J.; Wang, Z. *J. Phys. Chem. B* **2004**, *108*, 14005–14008.
(18) Wang, L.; Luo, J.; Fan, Q.; Suzuki, M.; Suzuki, I. S.; Engelhard, M. H.; Lin, Y.; Kim, N.; Wang, J. Q.; Zhong, C. J. *J. Phys. Chem. B* **2005**, *109*, 21593–21601.
(19) Park, H.; Schadt, M. J.; Wang, L.; Lim, I-I. S.; Njoki, P. N.; Kim, S. H.; Jang, M.; Luo, J.; Zhong, C. J. *Langmuir* **2007**, *23*, 9050–9056.
(20) Luo, J.; Wang, L.; Mott, D.; Njoki, P. N.; Lin, Y.; He, T.; Xu, Z.; Wanjana, B. N.; Lim, I. S.; Zhong, C. J. *Adv. Mater.* **2008**, *20*, 4342–4347.
(21) Rusakova, I.; Ould-Ely, T.; Hofmann, C.; Prieto-Centurion, D.; Levin, C. S.; Halas, N. J.; Luttge, A.; Whitmire, K. H. *Chem. Mater.* **2007**, *19*, 1369–1375.
(22) Han, S.; Li, C.; Liu, Z.; Lei, B.; Zhang, D.; Jin, W.; Liu, X.; Tang, T.; Zhou, C. *Nano Lett.* **2004**, *4*, 1241–1246.
(23) Hashimoto, A.; Suenaga, K.; Gloter, A.; Urita, K.; Iijima, S. *Nature* **2004**, *430*, 870–873.
(24) Geach, G. A.; Phillips, R. *Nature* **1957**, *179*, 1293–1293.
(25) Kishimoto, S.; Yamauchi, Y. *Phys. Chem. Chem. Phys.* **2009**, *11*, 5554–5557.
(26) Lee, Y.; Lee, J.; Bae, C. J.; Park, J. G.; Noh, H. J.; Park, J. H.; Hyeon, T. *Adv. Funct. Mater.* **2005**, *15*, 503–509.
(27) Wang, L.; Luo, J.; Maye, M. M.; Fan, Q.; Rendeng, Q.; Engelhard, M. H.; Wang, C.; Lin, Y.; Zhong, C. J. *J. Mater. Chem.* **2005**, *15*, 1821–1832.
(28) Zheng, Z.; Zhong, X.; Zhang, Y.; Yu, H.; Zeng, D. *J. Alloys Compd.* **2008**, *466*, 377–382.
(29) Dasgupta, S.; Kim, K. B.; Ellrich, J.; Eckert, J.; Manna, I. *J. Alloys Compd.* **2006**, *424*, 13–20.
(30) Gillot, B.; Buguet, S.; Kester, E.; Baubet, C.; Tailhades, P. *Thin Solid Films* **1999**, *357*, 223–231.
(31) Wang, C. M.; Baer, D. R.; Amonette, J. E.; Engelhard, M. H.; Qiang, Y.; Antony, J. J. *Nanotechnology* **2007**, *18*, 255603.
(32) Wang, C. M.; Baer, D.; Amonette, J.; Engelhard, M. H.; Antony, J. J.; Qiang, Y. *Ultramicroscopy* **2007**, *108*, 43–51.
(33) Wang, C. M.; Baer, D. R.; Thomas, L. E.; Amonette, J. E.; Antony, J. J.; Qiang, Y.; Duscher, G. *J. Appl. Phys.* **2005**, *98*, 094308.
(34) West, A. R. *Basic Solid State Chemistry*, 2nd ed.; Wiley: New York, 2000; p 388−391.
(35) Venkataraju, C.; Sathishkumar, G.; Sivakumar, K. *J. Alloys Compd.* **2010**, *498*, 203–206.
(36) Rao, A. D. P.; Raju, S. B.; Vadera, S. R.; Sharma, D. R. *Bull. Mater. Sci.* **2003**, *26*, 505–507.
(37) Grasset, F.; Labhsetwar, N.; Li, D.; Park, D. C.; Saito, N.; Haneda, H.; Cador, O.; Roisnel, T.; Mornet, S.; Duguet, E.; Portier, J.; Etourneau, J. *Langmuir* **2002**, *18*, 8209–8216.
(38) Park, J.; Lee, E.; Hwang, N. M.; Kang, M. S.; Kim, S. C.; Hwang, Y.; Park, J. G.; Noh, H. J.; Kini, J. Y.; Park, J. H.; Hyeon, T. *Angew. Chem., Int. Ed.* **2005**, *44*, 2872–2877.
(39) Puntes, V. F.; Krishnan, K. M.; Alivisatos, A. P. *Appl. Phys. Lett.* **2001**, *78*, 2187–2189.

JA1091084